

In-Home Monitoring Using Wireless on the Walls for Future HealthCare: Real-World Demonstration

Jalil ur Rehman Kazim,* Ahsen Tahir, James Rains, Tie Jun Cui, Abdul Jabbar, Muhammad Ali Jamshed, Masood Ur-Rehman, Akram Alomainy, Muhammad Ali Imran, and Qammer H. Abbasi

Since the last decade radio frequency (RF) sensing has emerged as an alternative in-home monitoring and tracking technology because of its inherent device-free and privacy-preserved features over camera and wearable technologies. In this work, contrary to conventional radar-based sensing and WiFi-based setups which require line-of-sight (LoS) to process and collect the RF signals for monitoring, it is shown for the first time in literature the potential of using RF sensing for vitals, that is, heartbeat detection in the non-line-of-sight (NLoS) using an in-house-developed reconfigurable intelligent surface (RIS), that is, wireless on the walls. The developed RIS is the world's first prototype which consists of "4096 elements". The unit cell elements are individually controlled via PIN diodes, 1-bit, operating at 3.75 GHz specified for the fifth-generation (5G) network. Near-field beam steering is demonstrated, with a switching speed of 15 ms. For the first time in the literature it is demonstrated that RIS can assist in the detection of microactivities including the human heartbeat in NLoS indoor complex environment, a limitation with the existing RF sensing technologies to date. In addition, it is experimentally verified that the RIS can potentially reduce the e-field magnitude at the user's by regulating the gain at the user terminal.

Communications (URLLC), that is, $5\times$ fewer delay optimized data.^[4–7] Novel technologies such as Extended Reality (XR),^[8] Holographic Telepresence,^[8] Unmanned Aerial Vehicles (UAV),^[9] smart grid 2.0,^[10] and Industry 5.0^[11] will become a key part of B5G/6G. To realize the above, breakthrough technologies such as Ultra-Massive Multiple-Input-Multiple-Output (UM-MIMO)^[12] and Cell-Free massive MIMO (CF-MIMO)^[13] and Terahertz (THz) communication^[14] will be adopted in future wireless systems. Additionally, a key pillar in the 6G communication ecosystem will include Integrated Sensing and Communication (ISAC) capabilities.^[15,16]

Applications such as high-speed mobile communication, high-precision positioning, gesture recognition, and real-time contactless health monitoring will be integrated into a single system thus enabling sophisticated solutions for future 6G scenarios, such as smart hospitals, smart homes, and smart vehicles.


High-speed mobile communication, localization and positioning, involve machine-to-machine communication, while gesture recognition and contactless health monitoring involve human interaction and high-precision sensing. Currently, the existing technology such as WiFi^[17,18] millimeter wave (mmWave)^[19,20] and THz^[21,22] are commonly adopted for sensing applications.

Leveraging the existing cellular signals to investigate sensing mechanisms and applications for the surrounding people,

1. Introduction

5G mobile communication networks have rapidly been deployed around the world.^[1] Industry and academia have started to envision the role of Beyond 5G (B5G) and Sixth-Generation (6G) wireless mobile communication systems.^[2,3] 6G will offer seamless access, enhanced Mobile Broadband (eMBB) with $1000\times$ higher data rates, Ultra-Reliable and Low-Latency

J. Kazim, A. Tahir, J. Rains, A. Jabbar, M. A. Jamshed, M. Ur-Rehman, M. A. Imran, Q. H. Abbasi
James Watt School of Engineering
University of Glasgow
Glasgow G12 8QQ, UK
E-mail: j.kazim.1@research.gla.ac.uk

 The ORCID identification number(s) for the author(s) of this article can be found under <https://doi.org/10.1002/aisy.202300007>.

© 2023 The Authors. Advanced Intelligent Systems published by Wiley-VCH GmbH. This is an open access article under the terms of the Creative Commons Attribution License, which permits use, distribution and reproduction in any medium, provided the original work is properly cited.

DOI: 10.1002/aisy.202300007

A. Tahir
Department of Electrical Engineering
University of Engineering and Technology
Lahore 54890, PK

T. J. Cui
State Key Laboratory of Millimetre Waves
Southeast University
Nanjing 210096, China

A. Alomainy
School of Electronic Engineering and Computer Science
Queens Mary University of London
London E1 4NS, UK

objects, and environment inside the network deployment region is one of the realistic and promising approaches suggested by the ISAC for a B5G/6 G network.^[23] The prevailing sensing technologies cannot be integrated with cellular technology, for example, WiFi has an entirely different architecture and communication protocol,^[24] while mmWave and THz sensing make use of specialized dedicated hardware transceivers and generate customized waveforms different from cellular signals. Moreover, they mainly operate in LoS scenarios, controlled lab environments, and with lower sensing ranges.^[25] On the contrary, cellular sensing has the potential to transform all mobile devices and base stations into distributed sensors for widespread environment perception. Cellular signals provide several benefits, including 1) greater range of coverage for indoor and outdoor applications, 2) an increased amount of time that base stations may remain operational, and 3) permitted frequency bands that can see less interference.

For sensing applications, the ambient cellular signals transmitted from the base station need to be focused and steered to the desired spot, that is, the target location, to eliminate the unwanted noise added from the environment. The focusing is made possible with phased arrays at the base station but becomes challenging if the human subject is in the NLoS. Also, the adaptation of mmWave and/or THz frequencies in future wireless communication will bring forth a significant challenge in the quest to establish ISAC system due to inherent limited propagation characteristics and the inability to provide coverages in NLoS. Consequently, this would require ultradense networks (UDNs)^[26] for coverage and high-power Massive MIMO antennas^[27] on the base station side, which would significantly raise the network cost at an exorbitant level and generate unnecessary electromagnetic fields in the environment.

A necessary solution to the aforementioned challenges would involve a low-cost, energy-efficient, beam-forming node that can simultaneously assist to extend the signal coverage as well as the sensing capabilities of communication system. In this regard, an emerging concept recently investigated is the reconfigurable intelligent surface (RIS).^[28,29] The RIS consists of many planar, low-cost, nearly passive reflecting elements with subwavelength spacing. The RIS can manipulate EM waves in desired directions. It is envisioned that RIS will play a key role in providing unobtrusive, contactless, future healthcare services.^[30] The most recent work concerning RIS-assisted sensing is the application in imaging for posture recognition.^[31–33] The author(s) have introduced a concept of learnt sensing to reduce unnecessary measurements for image reconstruction,^[31] while body posture and hand sign recognition is enabled using RIS as imager and recognizer with the help of machine learning.^[32,33] In another work, including RIS-assisted sensing, the author(s) have used frame configuration alternating optimization (FCAO) algorithm and a supervised learning algorithm for body posture recognition in a controlled lab environment.^[34] While posture and hand sign recognition involve static observation with little or no motion, our recent work demonstrates a significant advancement in real-time human activity monitoring in a complex propagating environment in NLoS enabled through RIS.^[35] The in-house prototype^[36] is developed for 5 G communication and demonstrates capabilities consistent with ISAC systems of the future. The proposed model was tailored to classify macroactivity movements

while microactivities including breathing and heart rate monitoring in real time were not addressed to date.

In this article, we present real-time vital monitoring of heartbeat, employing an in-house novel RIS testbed prototype developed for 5 G communication with the capability to focus in the near-field. The proposed RIS consumes low power, that is, 15 W with a higher switching speed, consisting of 4096 individually tuned, 1-bit elements. Measurements reveal that the RIS testbed prototype can steer the incoming beams in different directions operating at the 5 G frequency band. The RIS control mechanism is designed to compensate for the spherical wavefront sources placed in its near field, a feature not yet demonstrated by the recently published RIS prototypes at sub-6 GHz. We experimentally demonstrated three capabilities of the RIS: 1) RIS-enabled beamforming, 2) RIS-assisted micromovement sensing, and 3) RIS-assisted e-field exposure reduction in the uplink. We illustrate an accurate real-time heartbeat detection using the developed RIS prototype in the NLoS scenario. In addition, we have demonstrated that the proposed RIS can assist in reducing the e-field exposure at the user's terminal (in this case phantom head) in the uplink by gain adjustment through its aperture.

2. Unit Cell Modeling

The proposed unit cell model of the RIS is shown in **Figure 1**. From **Figure 1b**, it is shown that the PCB stackup is divided into two parts, that is, the RF layer and the control circuit layers. A 1-bit unit cell element shown in **Figure 1a** was designed and simulated using CST MWS studio software by exciting the reflecting element using a floquet port and the unit cell boundary condition.^[37] The unit cell element parameters are designed as follows: $W \times 1 = 22$ mm, $L \times 1 = 22$ mm, $W \times = 10.4$ mm, $L \times = 10.4$ mm, and $G = 0.2$ mm. The interelement spacing is kept around 22 mm. This is approximately a quarter wavelength at the center frequency of 3.75 GHz. A phase difference of 180° is achieved by shorting one portion of the patch with the ground through the RF p–i–n diode. An advantage of the proposed design is that the PIN diodes and the associated biasing circuits are placed on the bottom layer. This introduces ease of fabrication and eliminates EM scattering on the top layer due to interaction with the components and soldering material. The magnitude and phase response of the RIS was obtained in an anechoic chamber, details of which are provided in the “Experimental” Section. When the RF PIN diode is on, some inductance is introduced in the unit cell and the phase response over the operating bandwidth becomes positive, as shown in **Figure 1e**. In the switch-off state, there is only capacitance between the reflective patch and the RF ground plane. Furthermore, it is shown in **Figure 1d** that the simulated and measured magnitude response is around -3 dB, while the measured phase difference is around $180^\circ \pm 20^\circ$. The deviation in the simulated and measured phase response can be related to strong mutual coupling among the unit cells, which cannot be accurately modeled using ‘unit cell boundary’ conditions.^[38]

2.1. The Architecture of the Reconfigurable Intelligent Surface

The overall architecture of the RIS panel is shown in **Figure 2**. The designed RIS consists of 64×64 unit cells, that is, consisting

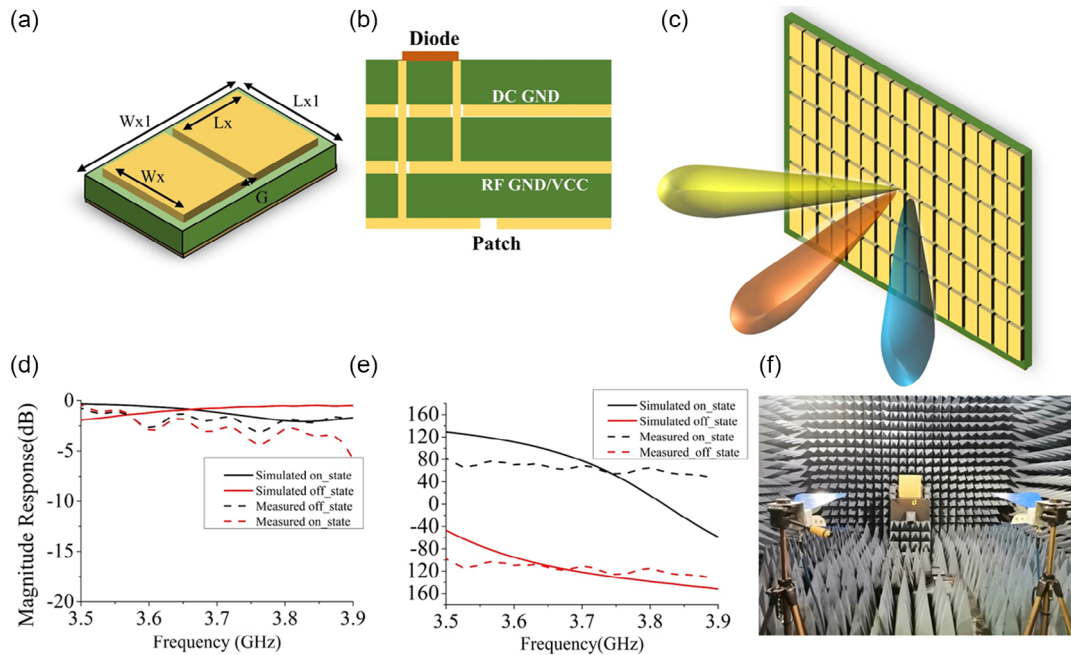


Figure 1. Architecture and unit cell response of the proposed RIS. a) Unit cell design of the proposed RIS, b) PCB layer stackup design, c) perspective view of the RIS, d) simulated and measured magnitude response, e) simulated and measured phase response, and f) experimental setup for the single RIS subarray.

of a total of 4096 elements. The complete RIS is divided into 16 subarrays. Each subarray has a dimension of $33 \times 33 \text{ cm}^2$. Hence, the total dimension of the RIS prototype is $132 \times 132 \text{ cm}^2$ which is $16.5 \lambda \times 16.5 \lambda$ at the operating frequency of 3.75 GHz. A 3 mm polycarbonate sheet with a size of $142 \times 142 \text{ cm}^2$ was installed on the aluminum frame stand and RIS subarrays were screwed on the polycarbonate sheet. Each subarray consists of 16×16 unit cell elements, which are individually connected using 16-bit, 16 light-emitting diode (LED) drivers cum shift registers (TLC5928DBQ). The LED drivers are connected in a daisy chain manner allowing data to flow serially in the subarray. Each single LED driver can drive 16 p-i-n diodes in parallel. Hence one single subarray accommodates 256 p-i-n diodes to switch between the two states. For voltage inputs and data transfer among the RIS subarrays, every single RIS subarray has one VDD, a negative, a clock, a data and a latch input line. These five lines also provide an output connection from the subarray and subsequently form input to succeeding subarrays. Hence, four subarrays are connected in a daisy chain configuration forming one single unit. This is depicted in Figure 2a.

The data transfer consisting of a clock and data line to the RIS is accomplished by connecting two of the single units to a single serial programming interface bus (SPI) from the Raspberry PI 3B+ controller with separate latch input to every single unit. Thus, two distinct but shared SPI connections (SPI0 and SPI1) perform data transfer to the RIS. The clock speed from the Raspberry was optimized at 7.8 MHz. The over-the-air data transfer takes place via a WiFi link from the algorithm running in MATLAB on the host PC. The Raspberry PI is configured to act as a WiFi hotspot, and a server program written in python accepts the incoming data from the MATLAB client. The server program passes the data to the

SPI pins connected to RIS. A single RIS configuration is transferred from the MATLAB program to the RIS in less than 15 ms.

2.2. Evaluation of RIS in Near Field

To validate the beam steering performance of the RIS, the measurements were performed by placing the source in the near-field region of the RIS. Initially, the simulated phase profile generated through MATLAB was transferred to the RIS. The transmitter distance in the simulation was taken as 1.5D and 0.5D, where 'D' corresponds to the overall dimension of the RIS, that is, 186 cm. The phase profile can be seen in Figure 2d–g, which forms a concentric gradient. For the beamsteering measurements, four scenarios were explored. The experimental setup and the calculation process is detailed in the "Experimental Section". Figure 2h–k shows the transmission (S_{21}) response over the frequency of 3.5–3.9 GHz. The experiment was performed in two steps. First, a precalculated phase profile was sent to the RIS for the transmitter position set at 0° and beam steered toward 25° and 40° . The measured results in Figure 2h,i show that the achieved gain (RIS off state to RIS optimized state) for the operating band, that is, 3.75 GHz is around 15–20 dB in 100 MHz bandwidth. The response in the rest of the bands was noted to be ≈ 10 dB. Similarly, in Figure 2j,k, the transmitter was offset from the 0° position to 15° and 25° and the receiver was kept at 25° and 40° alternatively. The measured gain, in this case, was around 10–15 dB in the operating band. The results indicate the effectiveness of the RIS in steering beams in different directions with the receiver and transmitter offset in the near field.

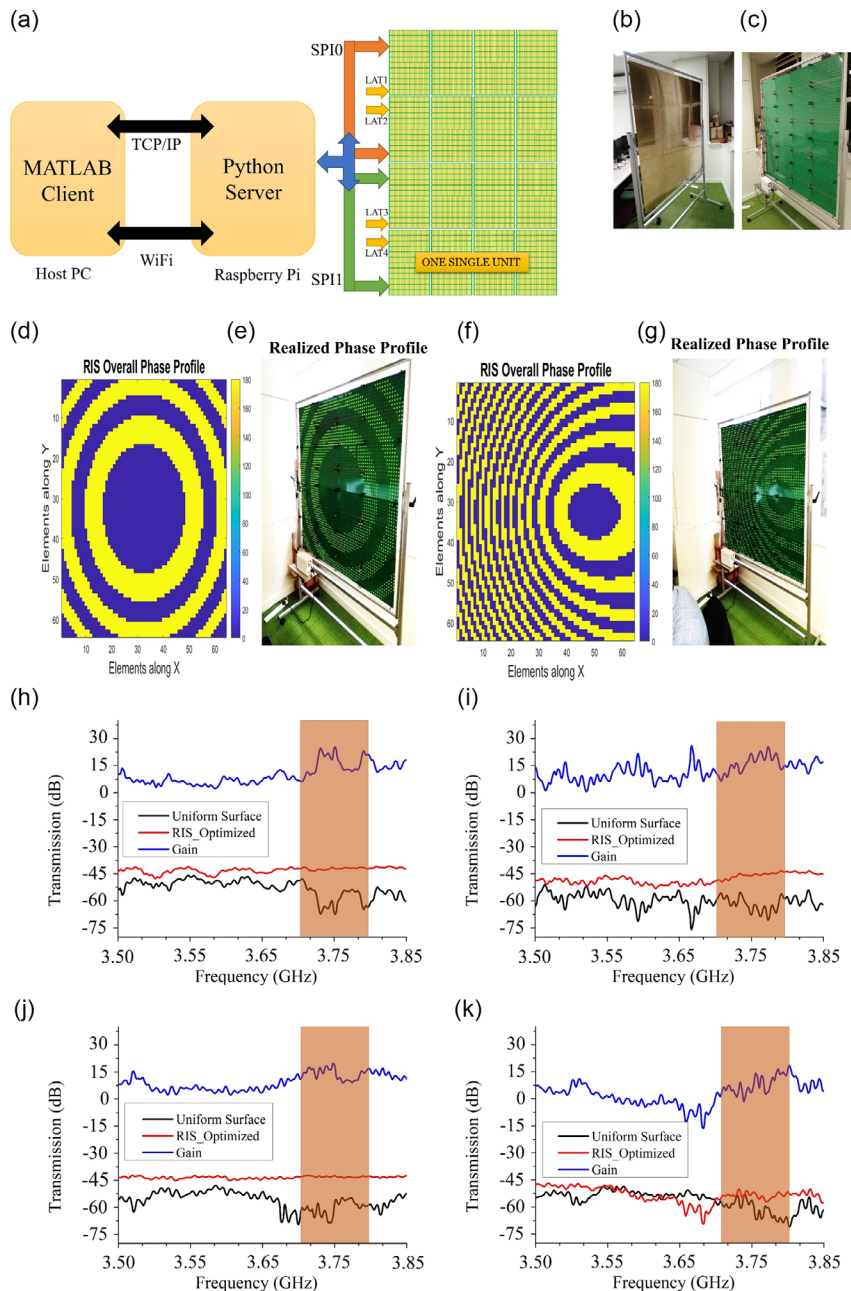


Figure 2. RIS architecture and performance evaluation. a) Information flow control to the RIS, b) fabricated RIS prototype with front view, c) back view, d) simulated phase distribution for broadside beam, e) implemented phase distribution for broadside beam, f) simulated phase distribution for 40° beam, g) implemented phase distribution 40° beams. h–k), Measured transmission response with RIS in switch-off state, optimized state, and achieved gain, that is, the difference between the off- and optimized state, with the location of h) T_x at 0° and R_x at 25°, i) T_x at 0° and R_x at 40°, j) T_x at 15° and R_x at 25° and T_x at 25°, and k) R_x at 40°.

3. RIS-Assisted Vital Signal Detection

RIS can assist with contactless vital signals detection by providing higher signal-to-noise ratios and greater distances of detection with non-line-of-sight (NLoS) monitoring of vitals. The ability to detect patient vital signs around objects and corners in the comfort of a patient’s space is an important distinction, which can be enabled by RIS-assisted RF sensing systems and

has been never done before. RIS-assisted vital signs detection consists of receiving the channel state information (CSI) corresponding to the same transmitted signal at the receiver antennas and taking the phase difference to remove random noise. The experimental setup is illustrated in **Figure 3** with details mentioned in the Experimental Section.

The sampling rate of 400 samples s^{-1} is utilized for CSI values from both antennas. The CSI signal must be pushed through

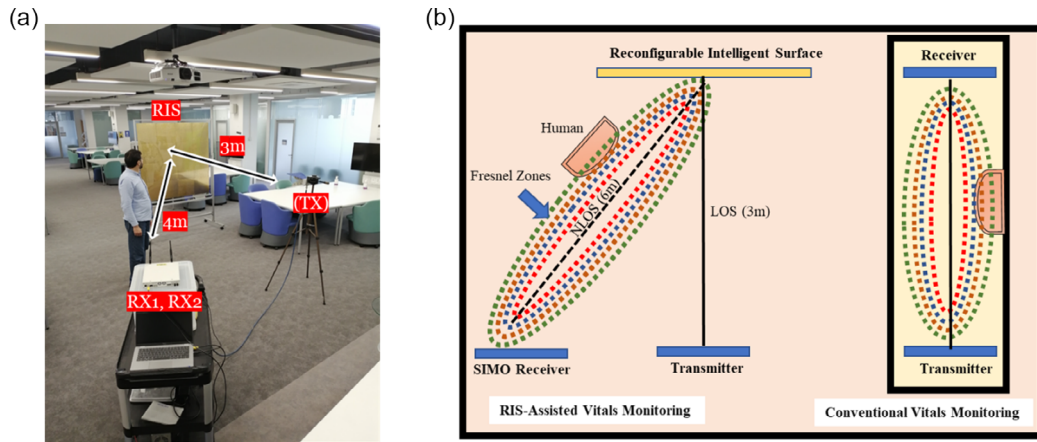


Figure 3. Experimental setup for the vital signals detection. a) Real-time measurement system for vitals detection. b) Conceptual model for vitals detection.

different filters to extract the required frequency components. A low-pass filter can be applied to remove reflection from static objects in the environment, while a high-pass filter is important to eliminate unwanted human motion from the signal. For instance, body motion associated with walking or running has a frequency range of $\approx 1\text{--}10$ Hz or higher. Hence, in the proposed work to extract the breathing rate and heart rate, a bandpass filter is utilized. The frequency response of the bandpass filter is kept from 0.1 to 0.5 Hz (12 beats/min to 16 beats min^{-1}) for the breathing rate^[39] and a bandpass filter from 1 to 2 Hz (60–120 beats min^{-1}) for the heart rate. A band stop filter is also

used in the range from 0.1 to 0.5 Hz before extracting the heart signal to remove any traces or higher-order harmonics from the breathing signals interfering with the heart signal because of its lower signal-to-noise ratio. The detection range from the transmitter is ≈ 7 m in the NLoS. The procedure is illustrated in **Figure 4**. Figure 4a represents the methodology adopted for heartbeat monitoring. The extracted heart and breathing rate signals obtained from utilizing the RIS are illustrated in Figure 4b,c.

The signals are estimated with good accuracy and have an error of less than 15% for both breathing and heart rates. The uncertainty arises from various sources including multipath

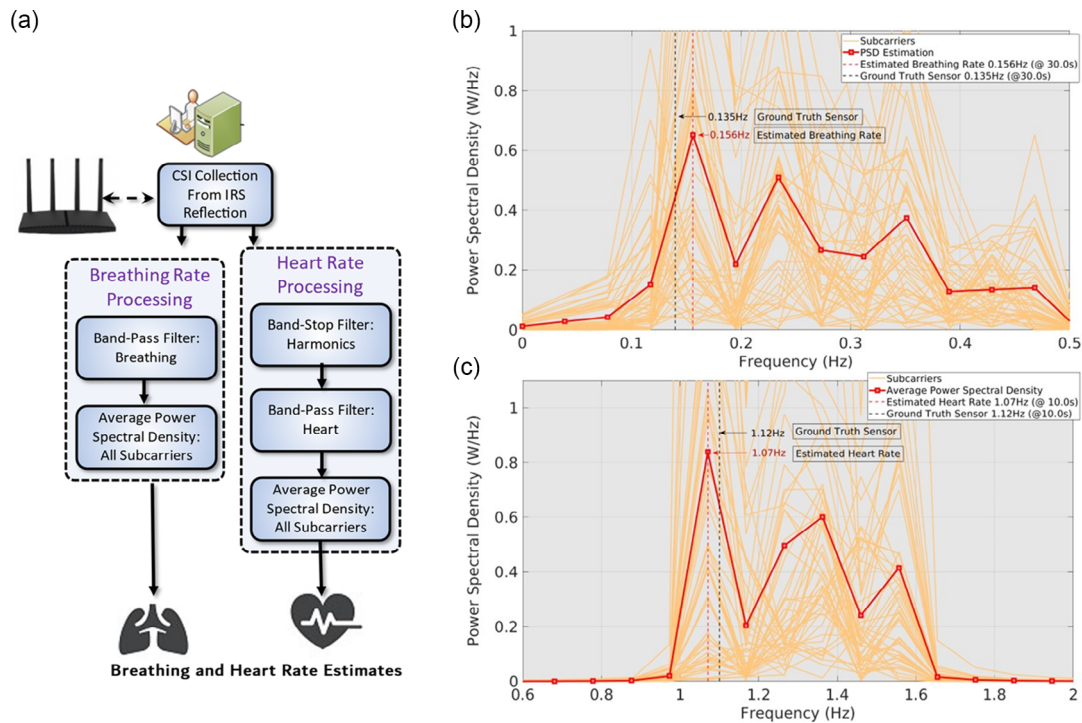


Figure 4. Methodology for heartbeat detection. a) Signal processing, b) heart rate from power spectral density (PSD) with ground truth H10 polar belt, c) Breathing rate from PSD with Vernier Go Direct breathing sensor as ground truth.

reflection from various objects, movements of objects, and the motion of the subject including movement of the chest due to breathing. The sampling rate and the resulting resolution of the Fast Fourier transform (FFT) and the PSD Watt/Hz measurements also affect the accuracy of the detected heart rate. The observed standard deviation error bar is 5.4% in mean accuracy, with the measurement window size of 10 s for the time domain CSI signal. The error increases with the decrease in size of the sampling window for the CSI signal measurement. The error in heart rate increases to standard deviation in mean value of 9.2% at 5 s and further deteriorates to 28.3% at 2.5 s window size. Thus, the utility of RIS in contactless vital signs detection has been demonstrated and results show a promising and viable alternative to the current intrusive sensors and methods, especially in NLoS.

4. E-Field Exposure Reduction by Aperture Control

The application of RIS relating to e-field reduction around the phantom head in the uplink channel is investigated and

demonstrated in this section. The RIS configuration algorithm adopted for the experiment is based on the adaptive optics-inspired approach employed by Gros et al.^[40] and is almost similar to the one utilized by Xilong et al.^[41] The experimental setup is shown in **Figure 5**. The setup is explained in detail in the “Experimental Section”.

A RIS configuration is sent involving flipping the bits of each unit cell at a time and comparing the received power level before and after each bit flip. This process is repeated until a given number of configurations are tested and maximum power is achieved. In this work, 300 iterations are considered for each measurement, with the resulting received power versus iteration. We have performed e-field measurements, where the number of addressable unit cells is limited to 24×24 , 32×32 , 48×48 , 56×56 , and 64×64 . The results are plotted in Figure 5d and the right-hand in same figure shows the achieved configuration profile. Initially, the transmitter gain was set to 19.7 dB and the RIS aperture size in terms of several usable elements was varied and the received power levels were noted. The dashed line at -55 dB power level shows the reference case for the unconfigured RIS, that is, RIS in the switch-off state. As illustrated in

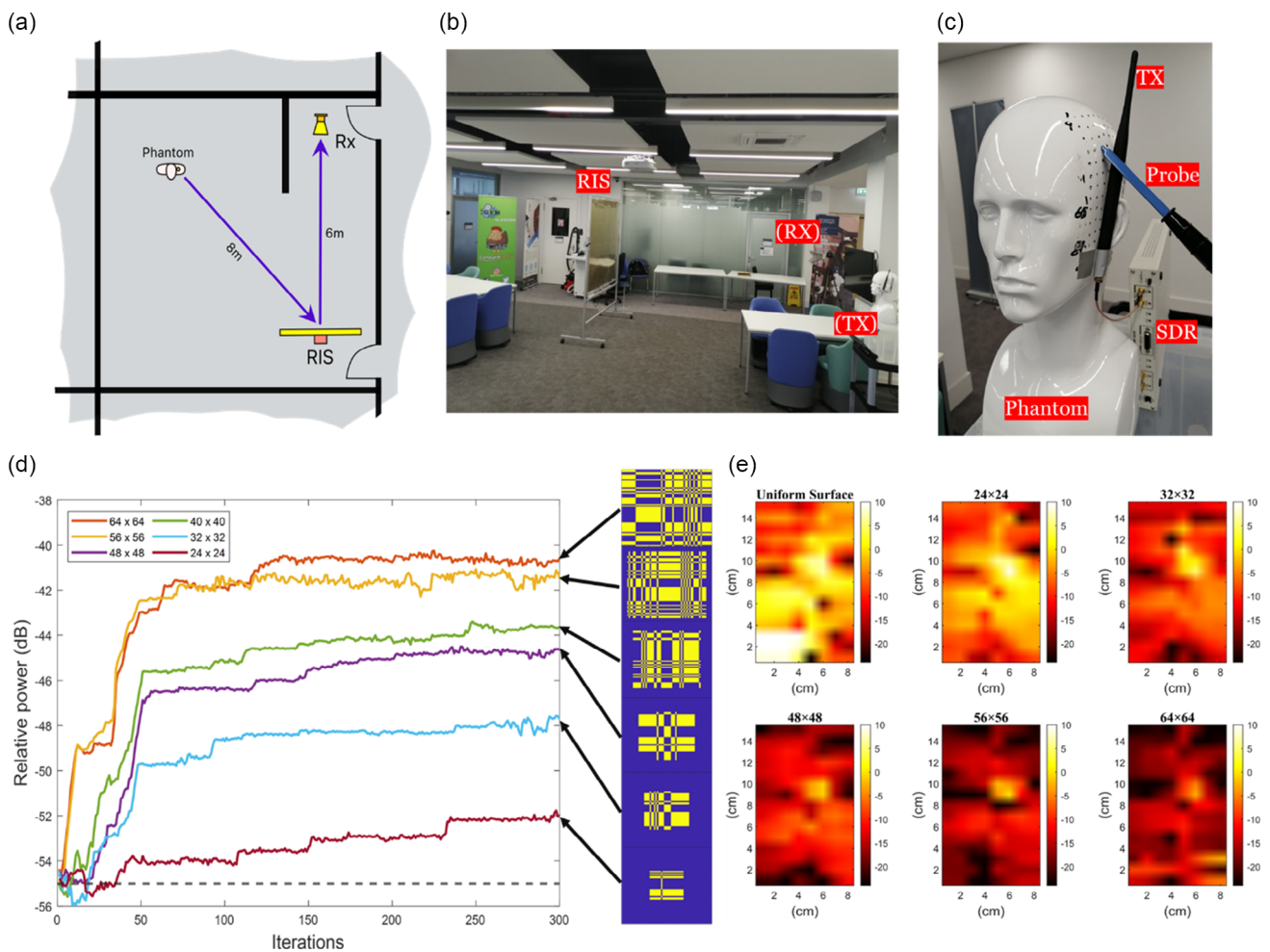


Figure 5. Experimental setup for e-field control. a) Measurement scenario. b) Uplink transmission setup using USRP X300. c) Probe for e-field measurement with the phantom. d) Measured received power level by varying the RIS aperture size along with configuration profiles on the right. The dashed line represents RIS as a uniform surface and e) measured e-field (dBV m^{-1}) distribution versus probe positions on the phantom head.

Table 1. Effect of RIS elements on the uplink transmitter gain.

RIS elements	Received power [dB] (Tx gain = 19.7 dB)	USRP T_x gain [dB] (received power threshold = -55 dB)	T_x Gain reduction [dB]
Uniform surface	-55	19.7	0
24 × 24	-51	15.7	4
32 × 32	-49	13.7	6
40 × 40	-45	9.7	10
48 × 48	-44	8.7	11
56 × 56	-41	5.7	14
64 × 64	-41.7	5	14.7

Figure 5d, the increase in RIS aperture size increases the measured power levels at the receiver. For the maximum usable elements of the RIS, that is, 64 × 64, the received power level observed was -41.7 dB. Then, the received power threshold was fixed to -55 dB and the RIS aperture size was iteratively increased. Consequently, the transmitter gain was decreased accordingly to maintain the received power threshold. The results are tabulated in Table 1.

Finally, the e-field plot over the phantom head was obtained for different aperture sizes while keeping the received power threshold at -55 dB. It can be seen in Figure 5e, the reference case (uniform surface), that is., off-state of the RIS, the e-field magnitude is maximum at the specified measured points on the phantom head, that is, when uplink transmitting gain is kept at a 19.7 dB. Thereafter, the RIS aperture size is varied with different unit cell elements optimized for maximum transmission. It can be seen in Figure 5e that the measured e-field is reduced around the phantom head, when RIS is optimized using the maximum number of unit cell elements, that is, 64 × 64 elements. In this case, the RIS provides a gain of around 14 dB from the switch-off state. Consequently, the transmitted gain in the uplink is reduced by 14 dB, that is, the transmitting gain is set to 5 dB resulting in reduced e-field. There is little noticeable difference between the 56 × 56 and 64 × 64 case, even though the 64 × 64 unit cell elements result in a 12.5% larger surface area control. This is advantageous as the lower number of unit cells will result in lower power consumption by the RIS and deliver the same performance.

The results indicate the role of RIS in controlling the E-field exposure around the phantom head, which directly impacts the specific absorption rate (SAR).^[42] SAR is an important parameter used to assess human tissue exposure to RF electromagnetic fields emitted from cellular phones in near-field regions. As SAR is directly proportional to the square of the E-field magnitude, it can be safely inferred that for a network operating with RIS deployments, the user handheld can safely operate with lower-than-expected SAR levels and as a result radiation effect would be minimized. Similarly, the effect of reduced uplink transmit power in the RIS-assisted communication scenario is the enhancement of the energy efficiency (EE) of the system. The EE of a wireless system is defined as the ratio of the system's throughput to the system's energy consumption

(EE = Throughput/Power Consumption). Therefore, EE can be increased by either maximizing system throughput or decreasing source transmit power.^[43] Here, since in the case of RIS-assisted communication, the source power consumption is drastically reduced (while assuming that the throughput and capacity of the system are not reduced), as a result, the EE of the communication system is anticipated to increase.

5. Conclusion

The RIS-assisted detection of vitals and e-field exposure control at user terminals in the uplink is one of the key applications investigated in this article in NLoS scenario while operating at 5 G frequency bands. For this purpose, we developed the world's first large intelligent reflective surface consisting of individually tuned, 1-bit, "4096-unit cell elements" at sub-6 GHz. The proposed prototype is scalable, operates with a high switching speed, that is, less than 15 ms per configuration, and consumes lower power, that is, 15 W during operation. Measured results demonstrate that the proposed RIS can focus the beam in different directions, making it capable to be used for tracking and in-house monitoring of elderly patients. Apart from the communication perspective, RIS-assisted healthcare is explored for the first time and envisioned to bring forth a paradigm shift in RF sensing technology for future healthcare.

6. Experimental Section

Operation of the RIS in Near Field: To analyze the radiation pattern which is formed in 3D space by an incoming signal bouncing back from the RIS, it is important to calculate the phase distribution profile. First, the array factor of "M" elements along the x-axis and "N" elements along the y-axis which shows a visual representation of the radiation property of any source was given by^[44]

$$AF_{xm} = \sum_{m=1}^M A_m e^{j(m-1)(kd_x \sin \theta \cos \phi + \beta_x + \phi_{comp})} \quad (1)$$

$$AF_{yn} = \sum_{n=1}^N A_n e^{j(n-1)(kd_y \sin \theta \sin \phi + \beta_y + \phi_{comp})} \quad (2)$$

Equation (1) and (2) represent the array factor of the element's position along the x and y-axis. Distance "dx" and "dy" are interelement spacing along the x and y-axis. The amplitude coefficients are represented by "A_m" and "A_n", respectively. Additionally, "k" represents the wavenumber which is cycles per unit length.

To steer the beam in a specific direction, it is essential to apply a progress phase shift which can be calculated using Equation (3) and (4). It is important to note that the phase shift "β_x" and "β_y" were independent of each other but for beam alignment, their values were kept the same.

$$\beta_x = -kd_x \sin \theta_0 \cos \phi_0 \quad (3)$$

$$\beta_y = -kd_y \sin \theta_0 \sin \phi_0 \quad (4)$$

Finally, the array factor of the 2D array was obtained by the product of array factors of the linear arrays along the x and y-direction specified in Equation (5).

$$AF = AF_{xm} \times AF_{yn} \quad (5)$$

To calculate the maximum directivity achieved by the RIS surface, a general expression given shown in Equation (6)^[44] is given as

$$D_0 = \frac{4\pi \cdot |AF(\theta_0, \phi_0)|^2}{\int_0^{2\pi} \int_0^\pi |AF(\theta, \phi)|^2 \sin \theta d\theta d\phi} \quad (6)$$

The transmitter location in the near field is a conventional example of RIS operating as a reflect array. This could be taken as zero if the source is placed in the far field. Assuming the position of the RIS elements as “ x_m ” and “ y_n ,” the phase compensation with respect to transmitter and RIS element location is given in Equation (7) as

$$\phi_{\text{comp}} = k \sqrt{(x_m - x_T)^2 + (y_n - y_T)^2 + z_T^2} - z_T \quad (7)$$

where m and n are equal to 0,1,2, 3,..., (M-1, N-1) such N is a total number of elements on the RIS. Also “ $x_T = T \sin(\theta_T) \cos(\phi_T)$,” “ $y_T = T \sin(\theta_T) \sin(\phi_T)$,” “ $z_T = T \cos(\theta_T)$ ” correspond to the source location at a distance “ T ” from the RIS.

Experimental Setup for RIS Measurement: This subsection explains the system configuration adopted during RIS measurements, which includes the RIS subarray magnitude and phase response and RIS beamsteering capability in the near field conducted in a large hall. For the evaluation of the magnitude and phase response of the proposed RIS, a subarray was placed in an anechoic chamber depicted in Figure 1f. The two transmitting and receiver horn antennas were placed at a distance of 3.5 m for the RIS subarray. At this distance, it was ensured that the antenna measurements were performed in the Fraunhofer region of the RIS subarray. The angular separation of the antennas from the center of the subarray was kept at 15° to avoid mutual coupling between the horn antennas. To calibrate the system and measure the magnitude and phase response of the RIS subarray, the transmission coefficient (S_{21}) was normalized by taking a metal plate equivalent to the size of the RIS subarray, that is, $33 \times 33 \text{ cm}^2$.

To perform the beam steering measurements, the RIS prototype was placed in a large hall. The transmitting horn was placed at a distance of 3 m at the broadside from the RIS, while the receiving horn was placed at 6 m at different angles for measurements. Once the RIS was loaded with a precalculated configuration for a particular beam direction using near-field equations given above, a portable VNA connected to both antennas through RF cables was used to measure the transmission response of the RIS. Figure 5h,i,j,k shows different transmission responses collected for various transmitter and receiver angles. The transmitted power from the VNA was set to 0 dBm with frequencies in the range of 3.5–3.9 GHz.

Experimental Setup for Vital Signals Detection: For real-time measurement of the vitals, that is heartbeat and breathing rate, two receivers were used to calculate the phase difference of the received signals bouncing off the chest. For this purpose, Universal Serial Radio Peripheral (USR) X300 was used, which was configured to capture signals on two channels. The same USRP was also configured to use as a transmitter. Hence, transmission and reception were performed using a single USRP. The gain was set to maximum for both transmit and receive channels, that is, 35 dB. The operating frequency was kept at 3.75 GHz. The transmitter was fixed at a distance of 3 m normal to the RIS, while the receiver was kept at 4 m at an angle of 30°. The heart rate monitoring was performed midway between the receiver and the RIS. A GNU radio program transmits OFDM signals and the receiver was set to collect 1000 samples per second. Ethical approvals were acquired under approval number: 300 200 232 from the University of Glasgow, before the data collection in this study.

Experimental Setup for e-Field Measurement: To validate the efficacy of RIS in reducing the e-field around the phantom head, TEKBOX electromagnetic compatibility (EMC) near-field probe (Model TBPS01) was used to perform e-field measurements. The experimental setup is shown in Figure 5a,b. The RIS was placed at 6 m and 8 m from the receiver horn antenna (Rx) and the transmitter monopole antenna (T_x) attached to the phantom. The RIS was positioned such that it was 6 m away normal to the R_x and 8 m, 45° relative to the T_x thus, creating a RIS-assisted communication link between the transmitter and the receiver. The T_x setup consisted of a laptop connected via an ethernet cable to a USRP X300 software radio with the T_x placed on the phantom ear, emulating the uplink of a mobile user. The R_x consisted of a standard gain horn antenna

connected to a USRP B205 mini via a USB cable to the laptop. The measurements were taken with the monopole antenna connected to the phantom head in transmission mode. The e-field probe was positioned close to the phantom shown in Figure 5c. The output of the probe was attached to a spectrum analyzer to detect the resultant power shown in Figure 5e. The data was collected in a grid of 120 points, arranged over an area of $90 \text{ mm} \times 160 \text{ mm}$ on the phantom, which is depicted in Figure 5c. Hence the grid was divided into 8 columns and 14 rows. Hence, a total of 120 measurements were taken using the probe. The gap between each point was kept at 10 mm. The e-field data was obtained using the following equation.

$$E = 10^{\frac{(P + 112.5 - 20 \log_{10} F)}{20}}$$

where “ E ” is the electric field strength, “ P ” is the probe output power in dBm, and “ F ” is the operating frequency in MHz.

Fabrication: The reflective patch was printed on top of a conductor-backed F4BM substrate ($\epsilon_r = 2.65$ and $\tan \delta = 0.004$ at 10 GHz) having a thickness of 1.527 mm. Two, 0.4 mm-thick FR-4 dielectric slabs ($\epsilon_r = 4.4$ and $\tan \delta = 0.02$ at 10 GHz) were glued using prepreg material underneath the reflective patch. The thickness of the copper metal was taken as 17 μm . Hence the overall thickness of the PCB board was around 2.4 mm. The first layer beneath the reflective patch acted as the positive VCC plane and served as power input to the LED drivers. The second layer beneath the VCC plane was assigned a negative DC plane which was connected to the diode’s negative junctions. The bottom layer consisted of an RF p-i-n diode (SMP 1345-079LF) and the LED driver (TLC5928DBQ) which were cascaded in a daisy-chain method to transfer bit states to the p-i-n diode. The positive junction of the p-i-n diodes was controlled with the LED drivers individually through 0.3 mm bias lines. The diode voltage was kept at 0.83 V which set the current to 1 mA. Consequently, the maximum power consumption of the RIS was measured to be 18 W when all diodes were in ON state.

Acknowledgements

This work was supported in parts by Engineering and Physical Sciences Research Council (EPSRC) grants: EP/T021020/1 and EP/T021063/1 and SAPHIRE 2022 grant no:2814 and ICRG PAK-UK Education Gateway (2020) funded Project No. 310366.

Conflict of Interest

the authors declare no conflict of interest.

Data Availability Statement

Data sharing is not applicable to this article as no new data were created or analyzed in this study.

Keywords

healthcare, intelligent reflect surfaces, radio frequency sensing, specific absorption rates

Received: February 2, 2023

Revised: May 3, 2023

Published online: July 8, 2023

[1] P. Popovski, K. F. Trillingsgaard, O. Simeone, G. Durisi, *IEEE Access* **2018**, 6, 55765.

[2] K. B. Letaief, W. Chen, Y. Shi, J. Zhang, Y. J. A. Zhang, *IEEE Commun. Mag.* **2019**, 57, 84.

- [3] M. A. Uusitalo, P. Rugeland, M. R. Boldi, E. C. Strinati, P. Demestichas, M. Ericson, G. P. Fettweis, M. C. Filippou, A. Gati, M. H. Hamon, M. Hoffmann, M. Latva-Aho, A. Pärssinen, B. Richerzhagen, H. Schotten, T. Svensson, G. Wikström, H. Wymeersch, V. Ziegler, Y. Zou, *IEEE Access* **2021**, 9, 160004.
- [4] M. Giordani, M. Polese, M. Mezzavilla, S. Rangan, M. Zorzi, arXiv:1903.12216, **2019**.
- [5] K. M. S. Huq, S. A. Busari, J. Rodriguez, V. Frasca, W. Bazzi, D. C. Sicker, *IEEE Netw.* **2019**, 33, 89.
- [6] W. Saad, M. Bennis, M. Chen, *IEEE Netw.* **2019**, 34, 134.
- [7] F. Tariq, M. Khandaker, K.-K. Wong, M. Imran, M. Bennis, M. Debbah, arXiv:1902.06700, **2019**.
- [8] M. Martin, E. Amin, *Toward 6G: A New Era of Convergence*, IEEE **2021**, pp. 167–182, <https://doi.org/10.1002/9781119658054.ch7>.
- [9] M. Mozaffari, X. Lin, S. Hayes, *IEEE Commun. Mag.* **2021**, 59, 74.
- [10] J. Cao, M. Yang, *IEEE Comp. Soc.* **2014**, 105.
- [11] S. Nahavandi, *Sustainability* **2019**, 11, 4371.
- [12] I. F. Akyildiz, J. M. Jornet, *Nano Commun. Netw.* **2016**, 8, 46.
- [13] E. Nayebi, A. Ashikhmin, T. L. Marzetta, H. Yang, in *49th Asilomar Conf. on Signals, Systems and Computers*, IEEE, Pacific Grove, CA, USA **2015**, pp. 695–699, <https://doi.org/10.1109/ACSSC.2015.7421222>.
- [14] V. Petrov, T. Kurner, I. Hosako, *IEEE Commun. Mag.* **2020**, 58, 28.
- [15] F. Liu, Y. Cui, C. Masouros, J. Xu, T. X. Han, Y. C. Eldar, S. Buzzi, *IEEE J. Select. Areas Commun.* **2022**, 40, 1728.
- [16] A. Liu, Z. Huang, M. Li, Y. Wan, W. Li, T. X. Han, C. Liu, R. Du, D. K. P. Tan, J. Lu, Y. Shen, F. Colone, K. Chetty, *IEEE Commun. Surveys Tutor.* **2022**, 24, 994.
- [17] A. Khalili, A.-H. Soliman, M. Asaduzzaman, A. Griffiths, *J. Eng.* **2020**, 2020, 87.
- [18] H. Hameed, M. Usman, A. Tahir, A. Hussain, H. Abbas, T. J. Cui, M. A. Imran, Q. H. Abbasi, *Nat. Commun.* **2022**, 13, 5168.
- [19] D. Liu, U. Pfeiffer, J. Grzyb, B. Gaucher, in *Advanced Millimeter-Wave Technologies: Antennas, Packaging And Circuits*, John Wiley & Sons, Hoboken, NJ **2009**.
- [20] B. V. Berlo, A. Elkelany, T. Ozcelebi, N. Meratnia, *IEEE Sens. J.* **2021**, 21, 10332.
- [21] X. Wu, H. Lu, K. Sengupta, *Nat. Commun.* **2019**, 10, 2722.
- [22] D. Saeedkia, in *Handbook Of Terahertz Technology For Imaging, Sensing And Communications*, Elsevier, Amsterdam **2013**.
- [23] Y. Chen, J. Zhang, W. Feng, M. S. Alouini, *IEEE Internet Things J.* **2022**, 9, 1037.
- [24] *IEEE Std 802.11-2020 (Revision of IEEE Std 802.11-2016) - Redline* **2021**, p. 1.
- [25] F. Zhang, Z. Chang, K. Niu, J. Xiong, B. Jin, Q. Lv, D. Zhang, *Proc. ACM Interact. Mob. Wear. Ubiqu. Technol.* **2020**, 4, 68.
- [26] R. Baldemair, T. Irnich, K. Balachandran, E. Dahlman, G. Mildh, Y. Selén, S. Parkvall, M. Meyer, A. Osseiran, *IEEE Commun. Mag.* **2015**, 53, 202.
- [27] E. G. Larsson, O. Edfors, F. Tufvesson, T. L. Marzetta, *IEEE Commun. Mag.* **2014**, 52, 186.
- [28] T. J. Cui, M. Q. Qi, X. Wan, J. Zhao, Q. Cheng, *Light: Sci. Appl.* **2014**, 3, 218.
- [29] Q. Ma, G. D. Bai, H. B. Jing, C. Yang, L. Li, T. J. Cui, *Light: Sci. Appl.* **2019**, 8, 98.
- [30] J. U. R. Kazim, T. J. Cui, A. Zoha, L. Li, S. A. Shah, A. Alomainy, M. A. Imran, Q. H. Abbasi, *IEEE Antennas Propag. Mag.* **2021**, 63, 87.
- [31] H. Y. Li, H. T. Zhao, M. L. Wei, H. X. Ruan, Y. Shuang, T. J. Cui, P. del Hougne, L. Li, *Patterns* **2020**, 1, 100006.
- [32] L. Li, Y. Shuang, Q. Ma, H. Li, H. Zhao, M. Wei, C. Liu, C. Hao, C. W. Qiu, T. J. Cui, *Light: Sci. Appl.* **2019**, 8, 97.
- [33] L. Li, H. Ruan, C. Liu, Y. Li, Y. Shuang, A. Alù, C. W. Qiu, T. J. Cui, *Nat. Commun.* **2019**, 10, 1082.
- [34] J. Hu, H. Zhang, B. Di, L. Li, K. Bian, L. Song, Y. Li, Z. Han, H. V. Poor, *IEEE J. Select. Areas Commun.* **2020**, 38, 2700.
- [35] M. Usman, J. Rains, T. J. Cui, M. Z. Khan, J. U. R. Kazim, M. A. Imran, Q. H. Abbasi, *Light: Sci. Appl.* **2022**, 11, 212.
- [36] J. Rains, J. U. R. Kazim, A. Tukmanov, T. J. Cui, L. Zhang, Q. H. Abbasi, M. A. Imran, *IEEE Trans. Antennas Propag.* **2022**, 71, 518.
- [37] J. U. R. Kazim, M. Ur-Rehman, M. Al-Hasan, I. B. Mabrouk, M. A. Imran, Q. H. Abbasi, in *Int. Conf. on UK-China Emerging Technologies (UCET)*, IEEE, Piscataway, NJ **2020**, pp. 1–4.
- [38] S. An, B. Zheng, M. Y. Shalaginov, H. Tang, H. Li, L. Zhou, Y. Dong, M. Haerinia, A. M. Agarwal, C. Rivero-Baleine, M. Kang, K. A. Richardson, T. Gu, J. Hu, C. Fowler, H. Zhang, *Adv. Opt. Mater.* **2022**, 10, 2102113.
- [39] B. Hill, S. H. Annesley, *Br. J. Nurs.* **2020**, 29, 12.
- [40] J. B. Gros, V. Popov, M. A. Odit, V. Lenets, G. Lerosey, *IEEE Open J. Commun. Soc.* **2021**, 2, 1055.
- [41] X. Pei, H. Yin, L. Tan, L. Cao, Z. Li, K. Wang, K. Zhang, E. Björnson, *IEEE Trans. Commun.* **2021**, 69, 8627.
- [42] R. E. Fields, *OET Bull.* **1997**, 65.
- [43] M. S. Syam, S. Luo, Y. L. Che, K. Wu, V. C. M. Leung, *IEEE Syst. J.* **2022**, 1.
- [44] C. A. Balanis, in *Antenna Theory: Analysis And Design*, John Wiley & Sons, Hoboken, NJ **2015**.